Perovskites

International Edition: DOI: 10.1002/anie.201910471
German Edition: DOI: 10.1002/ange.201910471

Unconventional Route to Oxygen-Vacancy-Enabled Highly Efficient Electron Extraction and Transport in Perovskite Solar Cells

Bing Wang, Meng Zhang, Xun Cui, Zewei Wang, Matthew Rager, Yingkui Yang, Zhigang Zou, Zhong Lin Wang,* and Zhiqun Lin**

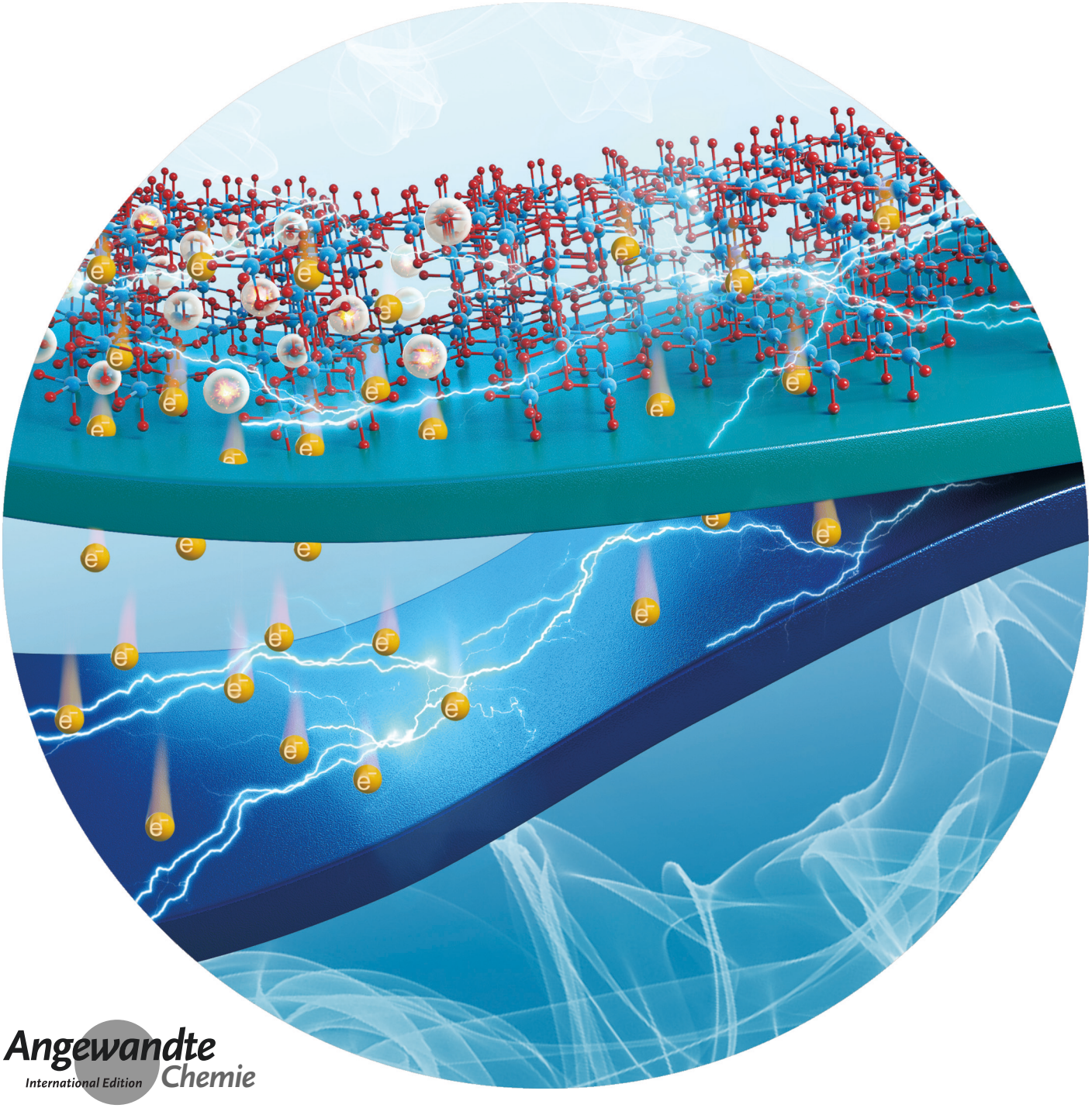

Angewandte International Edition Chemie

Abstract: *The ability to effectively transfer photoexcited electrons and holes is an important endeavor toward achieving high-efficiency solar energy conversion. Now, a simple yet robust acid-treatment strategy is used to judiciously create an amorphous TiO_2 buffer layer intimately situated on the anatase TiO_2 surface as an electron-transport layer (ETL) for efficient electron transport. The facile acid treatment is capable of weakening the bonding of zigzag octahedral chains in anatase TiO_2, thereby shortening staggered octahedron chains to form an amorphous buffer layer on the anatase TiO_2 surface. Such amorphous TiO_2-coated ETL possesses an increased electron density owing to the presence of oxygen vacancies, leading to efficient electron transfer from perovskite to TiO_2. Compared to pristine TiO_2-based devices, the perovskite solar cells (PSCs) with acid-treated TiO_2 ETL exhibit an enhanced short-circuit current and power conversion efficiency.*

Introduction

Recent research has witnessed rapid advances in metal halide perovskite materials and device due to their stellar set of optoelectronic properties.[1] Among various metal halide perovskite solar cells (PSCs), a certified power conversion efficiency (PCE) of 24.2% has been achieved in organic–inorganic hybrid PSCs.[2] One of the key steps to yielding high-performance PSC is to delicately control over the carrier transport from the perovskite absorber to the respective electrodes through charge transport layers (electron transport layer (ETL) and hole transport layer (HTL)).[3] The prerequisites for an ideal charge transport material involve a suitable energy level, high conductivity, and low surface recombination rate. TiO_2 is the most commonly used ETL in PSCs.[4] It is important to note that the surface of TiO_2 layer as well as the interface between TiO_2 and perovskite greatly impact the device performance.[4,5] However, nanometer-scale nonuniformities (for example, pinholes and resistive crystal boundaries that act as the charge recombination centers, namely, trap states) inevitably form on the crystalline TiO_2 surface during the sintering process, leading to direct contact between the perovskite absorber and electrodes.[6] The trap sites are recognized as interfacial barriers and consequently deteriorate the photovoltaic efficiency. In this context, much effort has been made to engineer the TiO_2 ETL/perovskite interface for promoting electron extraction and transport by passivating the surface traps and suppressing the charge recombination (for example, interface modification by n-doping TiO_2 with inorganic materials,[6a,7] and bridging TiO_2 and perovskite using organic coupling molecules[1b,8]). However, the use of inorganic or organic compounds as the bridge may reduce the interaction between TiO_2 and perovskite owing to the large dissimilarity in the chemical structures between TiO_2 and these compounds.[7] Clearly, it is highly desirable to develop a simple yet effective interfacial engineering approach to intimately connect TiO_2 and perovskite for efficient electron transfer. This has yet to be largely explored.

Oxygen vacancies and the Ti^{3+} state play a critical role in determining the surface and electronic properties of TiO_2.[8,9] They collectively render TiO_2 more conductive due to n-type doping as well as increased carrier density, thereby suppressing tunneling barriers and increasing photocurrent.[10] It is noteworthy that oxygen-deficient TiO_2 samples deliver superior performance as the improved conductivity induced by oxygen vacancies compensates the negative impact of trapping carriers that leads to inefficient electron transport.[11] Recently, an amorphous TiO_2 coating on the surface of Si photoanodes was found to effectively prevent corrosion and promote charge conduction due to its electric leakiness.[9a] Quite intriguingly, rather than forming a thin insulating barrier layer, the amorphous TiO_2 layer loses its lattice order with the generation of electronic defects, thus entailing the passage of high current densities.[9a] Notably, such an amorphous TiO_2 layer has been implemented for applications in photocatalysis,[9c] photoelectrochemistry,[8,9] lithium batteries,[9d] and quantum dots-sensitized solar cells.[9e] In contrast, investigation into the introduction of an amorphous layer in PSCs for enhancing device performance enabled by improved charge transport is surprisingly few and limited in scope.

Herein, we report on a robust strategy to deliberately create an amorphous TiO_2 layer at the interface between crystalline TiO_2 ETL and perovskite in PSCs resulting in markedly improved short circuit current J_{SC} and PCE. The acid treatment of TiO_2 ETL weakens the bonding of interconnected zigzag TiO_6 octahedral chains in anatase TiO_2, thereby shortening the staggered octahedron chains and rendering the formation of an amorphous TiO_2 buffer layer on the surface of anatase TiO_2. This amorphous TiO_2 buffer layer contains rich oxygen vacancies, as evidenced by EPR, XPS, and Mott–Schottky analysis, where the Mott–Schottky study reveals that the donor density of acid-treated TiO_2 ETL increases by one order of magnitude ($2.4\times10^{20}\,cm^{-3}$) compared to pristine TiO_2 ETL ($2.8\times10^{19}\,cm^{-3}$). The mixed cation–halide perovskite $Cs_{0.06}FA_{0.79}MA_{0.15}Pb(I_{0.85}Br_{0.15})_3$ is chosen as the light absorber and deposited on the amorphous TiO_2-coated ETL. Despite its amorphous nature, the amorphous TiO_2 buffer layer positioned at the interface of anatase TiO_2 and $Cs_{0.06}FA_{0.79}MA_{0.15}Pb(I_{0.85}Br_{0.15})_3$ effectively improves the electron diffusion and transport, as substantiated by electro-

[*] Dr. B. Wang, Dr. M. Zhang, Dr. X. Cui, Z. Wang, M. Rager, Prof. Z. L. Wang, Prof. Z. Lin
School of Materials Science and Engineering
Georgia Institute of Technology
Atlanta, GA 30332 (USA)
E-mail: zhong.wang@mse.gatech.edu
zhiqun.lin@mse.gatech.edu
Dr. B. Wang, Prof. Z. Zou
Eco-materials and Renewable Energy Research Center, National Laboratory of Solid State Microstructures, School of Physics
Nanjing University, Nanjing 210093 (P. R. China)
Dr. X. Cui, Prof. Y. Yang
Key Laboratory of Catalysis and Energy Materials Chemistry of Ministry of Education & Hubei Key Laboratory of Catalysis and Materials Science, South-Central University for Nationalities
Wuhan 430074 (China)
E-mail: ykyang@mail.scuec.edu.cn
Supporting information and the ORCID identification number(s) for the author(s) of this article can be found under: https://doi.org/10.1002/anie.201910471.

chemical impedance spectroscopy and controlled intensity-modulated photocurrent spectroscopy studies, leading to enhanced J_{SC} and PCE.

Results and Discussion

Figure 1a depicts the stepwise formation of acid-treated mesoporous TiO_2 film. Scanning electron microscopy (SEM) images of mesoporous TiO_2 before and after hydrochloric acid (HCl) treatment are shown in Figure 1b and c, respectively, where the HCl-treated TiO_2 film is seen to be more uniform with smaller and denser mesopores. The corresponding high-resolution transmission electron microscopy (HRTEM) images reveal that highly ordered anatase TiO_2 (Figure 1d) with well-resolved lattice fringes ($d = 0.352$ nm, corresponding to the (101) plane of anatase, JCPDF No. 21-1272; XRD patterns shown in the Supporting Information, Figure S1) becomes disordered after HCl soaking, displaying a smeared structure (Figure 1e) along with the film color turning black. This suggests a thin amorphous TiO_2 layer formed on the surface of anatase TiO_2 nanoparticles, and some disorder may also be generated within the nanoparticle. The disordered structures may be associated with the assembly of short staggered Ti–O octahedral chains (that is, forming amorphous TiO_2) resulted from the acid corrosion of TiO_2 crystal framework.[12] These chains are characteristic of amorphous TiO_2, particularly at the boundaries of adjacent crystalline TiO_2 nanoparticles.[13] Thus, the formation of a denser mesoporous HCl-treated TiO_2 film can be attributed to the reorganization of the Ti-O chains by acid that generates an amorphous TiO_2 buffer layer (marked in red; inset in the lower right panel in Figure 1a) intimately situated on the surface of crystalline TiO_2 nanoparticles (marked in green).[14]

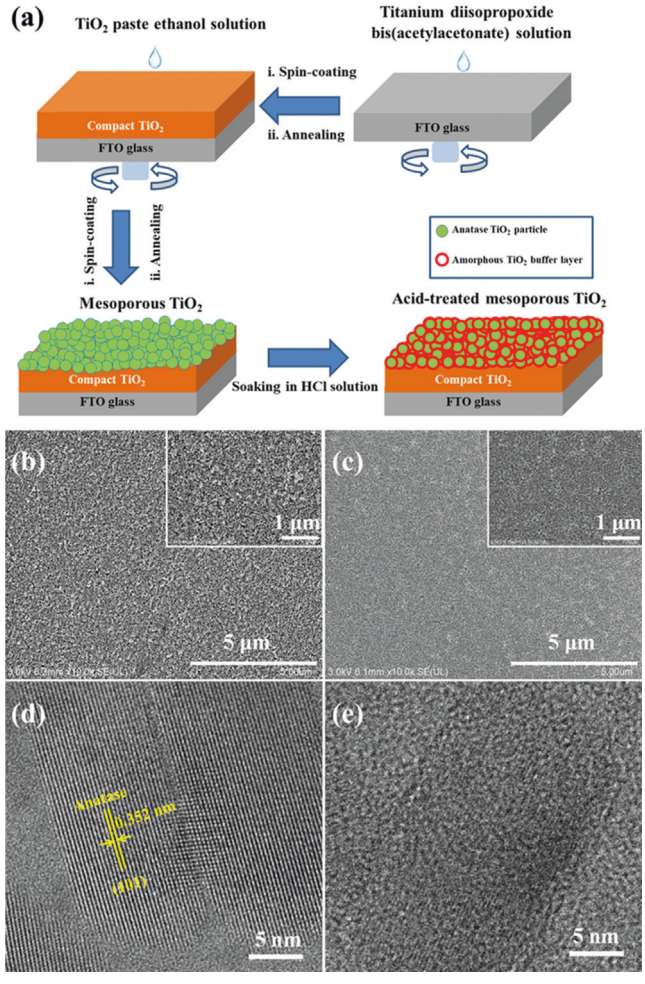

Figure 1. a) Illustration of the formation of amorphous TiO_2 buffer layer-coated anatase TiO_2 film via simple acid treatment. b, c) SEM images of mesoporous TiO_2 film (b) before and (c) after HCl treatment (top view). Insets show the close-ups. d, e) HRTEM images of mesoporous TiO_2 film (d) before and (e) after HCl treatment.

XPS measurement was conducted to determine the changes of TiO_2 surface states. Figure 2a compares the Ti 2p and O 1s core level spectra of pristine anatase TiO_2, and anatase TiO_2 after HCl treatment (denoted TiO_2-HCl) without and with subsequent plasma exposure. We note that O_2 plasma treatment was performed because the TiO_2-HCl film contains both surface and bulk (within TiO_2 nanoparticle; lower right in Figure 1a) oxygen vacancies, both of which increase the donor density of TiO_2 when employed as the ETL in PSC.[15] The bulk vacancies improve the bulk conductivity, while the surface vacancies trigger the charge carrier recombination.[16] Thus, removing surface vacancies yet retaining bulk vacancies in TiO_2 ETL by O_2 plasma exposure may lead to further improved performance of PSCs owing to suppressed photogenerated electron–hole recombination and the enhanced bulk conductivity. This will be discussed in detail later. Nonetheless, all the samples noted above exhibit the O 1s peak at approximately 531 eV, corresponding to the characteristic peak of Ti–O–Ti.[10] The O 1s peaks shift to high binding energy after HCl treatment yet without subsequent O_2 plasma exposure, and the O/Ti ratio on the TiO_2 surface decreases from 2.20 to 1.88 (Figure 2c), indicating that oxygen vacancies are generated on the surface of TiO_2-HCl nanoparticles (without plasma treatment). Generally, oxygen vacancies exist in the following three charge states: neutral, singly ionized, and doubly ionized,[17] as shown below:

i) Neutral oxygen vacancies:

$$O^{2-} \rightarrow 1/2\,O_2 + V_O \quad (1)$$

ii) Singly ionized vacancies:

$$O^{2-} \rightarrow 1/2\,O_2 + V_O' + e^- \quad (2)$$

$$Ti^{4+} + e^- \rightarrow Ti^{3+} \quad (3)$$

iii) Doubly ionized vacancies:

$$O^{2-} \rightarrow 1/2\,O_2 + V_O''v + 2\,e^- \quad (4)$$

$$2\,Ti^{4+} + 2\,e^- \rightarrow 2\,Ti^{3+} \quad (5)$$

One electron from a singly ionized oxygen vacancy or two electrons from a doubly ionized oxygen vacancy can be located at the neighboring Ti sites, leading to the formation of

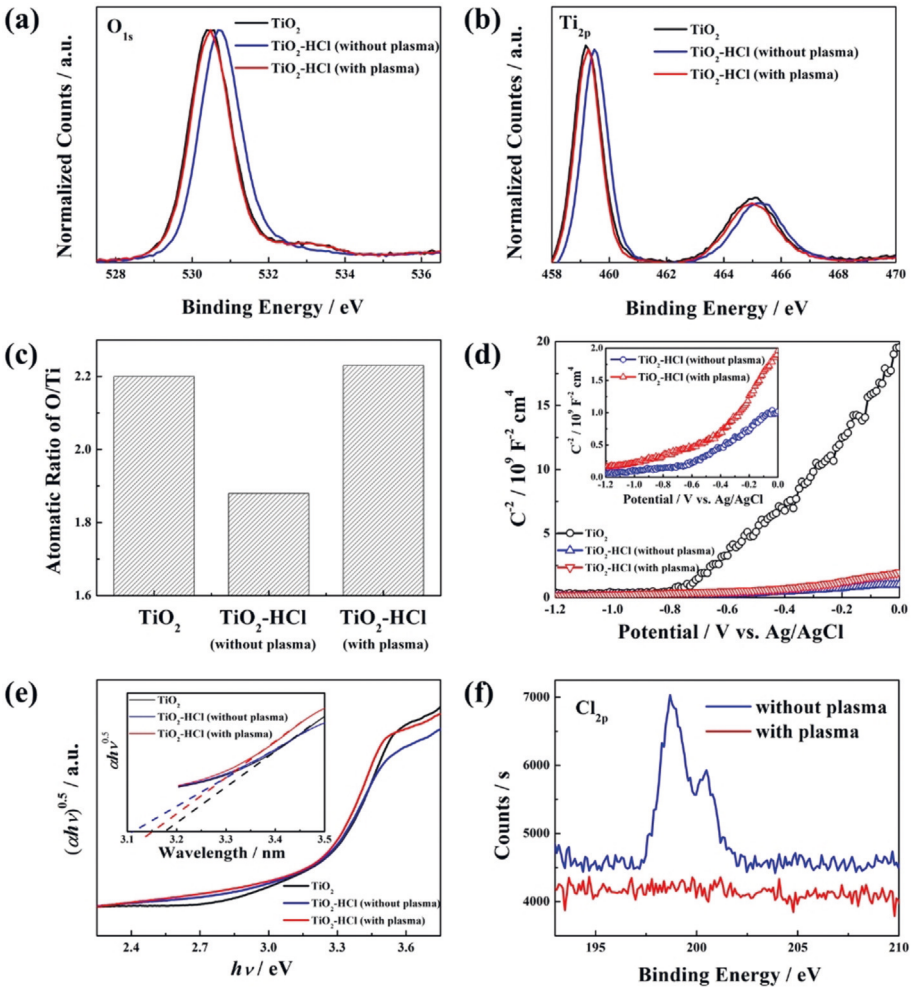

Figure 2. a) O 1s and b) Ti 2p core level spectra of TiO_2 and TiO_2-HCl films with and without subsequent O_2 plasma treatment. c) The O/Ti atom ratios of TiO_2 and TiO_2/HCl with and without O_2 plasma treatment. d) Mott–Schottky plots of TiO_2 and TiO_2-HCl films with and without plasma treatment at 5 kHz. e) Tauc plots of TiO_2 and TiO_2-HCl films with and without O_2 plasma treatment. f) Cl 2p core level spectra of TiO_2-HCl with and without O_2 plasma treatment.

Ti ions with lower state (that is, Ti^{3+}).[18] For a neutral oxygen vacancy, however, two electrons remain at the oxygen vacancy site, therefore, the neighboring Ti^{4+} oxidation states stay unchanged.[18] Compared to the neutral oxygen vacancy, the singly ionized and doubly ionized ones have larger lattice relaxation effect which changes the binding energy of O 1s and Ti 2p.[19] Thus, the peak shift of O 1s and Ti 2p to higher binding energy can be ascribed to the formation of singly ionized and doubly ionized oxygen vacancies. The singly ionized oxygen vacancies occupied by one electron has a spin of $S = 1/2$ and is thus paramagnetic.[20] A typical electron paramagnetic (EPR) signal at $g = 2.003$ (Supporting Information, Figure S2) provides direct evidence that singly ionized oxygen vacancies are created on the acid-treated TiO_2 samples.[21] Compared to O–Ti^{4+}, the O–Ti^{3+} bonds accompanied with the ionized oxygen vacancies reduce the electron charge density which decreases the screening effect of the O 1s outer electrons and increases the effective nuclear charge.[22] Consequently, the O 1s binding energy increases from 530.4 eV to 530.7 eV after HCl treatment yet without subsequent exposure to plasma. The binding energy of Ti 2p (459.6 eV) on TiO_2-HCl slightly deviates from the pristine TiO_2 film (459.3 eV), which may be a result of a correct stoichiometry owing to the formation of oxygen vacancies and Ti^{3+} in amorphous TiO_2 structure.

Depending on the location of oxygen vacancies in TiO_2, they can be classified as surface vacancies and bulk vacancies. The bulk vacancies improve the conductivity within the nanoparticles substantially as well as the electrical contact between nanoparticles.[15] While the surface vacancies also promote the surface conductivity, they do not largely contribute to the intrinsic electronic conductivity of TiO_2.[15] In contrast to the bulk oxygen vacancies, the surface oxygen vacancies aggravate charge carrier recombination as they act as surface trap sites.[23] Therefore, enhanced device performance is expected if surface oxygen vacancies are removed while bulk oxygen vacancies are retained in TiO_2 ETLs. To this end, we used O_2 plasma to treat the surface of TiO_2.[24] After plasma treatment, both O 1s and Ti 2p peaks of TiO_2-HCl (Figures 2a and b, respectively) overlap with the

corresponding peaks in pristine anatase TiO_2, suggesting that the surface oxygen vacancies generated in TiO_2-HCl are refilled upon the plasma treatment (yet bulk oxygen vacancies are remained, as disclosed by Mott–Schottky analysis discussed later). This finding can also be proven by XPS measurement of the O/Ti ratio on the TiO_2-HCl surface, which increases from 1.88 to 2.23 after plasma treatment. Moreover, the peak ratio change evidenced by Raman measurement (guided by straight lines; Supporting Information, Figure S3), which is resulted from the modified geometric and surface structures, also implies the presence of surface oxygen vacancies in TiO_2-HCl (without plasma) yet their removal in TiO_2-HCl (with plasma) samples.[25]

To substantiate that O_2 plasma treatment can retain the bulk vacancies in TiO_2-HCl, Mott–Schottky analysis was performed.[26] Based on the Mott–Schottky plots, the donor density N_D for the TiO_2-HCl film without plasma treatment was calculated to be $3.6\times10^{20}\,cm^{-3}$ (see Note 1 in the Supporting Information), which is comparable to the value of $2.4\times10^{20}\,cm^{-3}$ for TiO_2-HCl with plasma treatment. However, these values are one order of magnitude higher than that of the pristine anatase TiO_2 film ($N_D=2.8\times10^{19}$). As the surface oxygen vacancies are eliminated in the plasma-treated TiO_2-HCl sample, its larger N_D ($2.4\times10^{20}\,cm^{-3}$) should originate primarily from the bulk oxygen vacancies which are known as electron donors.[27] Taken together, it can be rationalized that oxygen vacancies in TiO_2 induced by acid treatment exist both on the surface and within the bulk TiO_2 nanoparticle in the TiO_2-HCl film, and the bulk oxygen vacancies are not abstracted upon the plasma treatment. The UV/Vis spectra further support this conclusion (Supporting Information, Figure S4), where the absorption edge of TiO_2-HCl in the presence of plasma treatment red-shifts compared to that of pristine TiO_2 owing to the generation of both surface and bulk oxygen vacancies (Figure 2e). As the surface oxygen vacancies are extracted, the band gap of TiO_2-HCl becomes larger after plasma treatment, but smaller than that of the pristine TiO_2 owing to the presence of bulk oxygen vacancies. Thus, compared to the TiO_2-HCl (without plasma)-based and the pristine TiO_2-based devices, the improved J_{SC} of the device constructed by capitalizing on plasma-treated TiO_2-HCl as ETLs (Supporting Information, Figure S5) is a direct consequence of the suppressed photogenerated electron–hole recombination and enhanced bulk conductivity owing to the presence of bulk oxygen vacancies. Unless otherwise specified, all the TiO_2-HCl samples discussed in the following are treated by plasma (Figure 3, Figure 4, Figure 5; Supporting Information, Figures S7–S13).

The morphology and optical properties of the $Cs_{0.06}FA_{0.79}MA_{0.15}Pb(I_{0.85}Br_{0.15})_3$ perovskite absorber deposited on pristine anatase TiO_2 and TiO_2-HCl films as ETLs are compared. Despite the distinct change in surface structure of TiO_2 before and after HCl treatment (Figure 1b,c), the morphology of the perovskite crystals deposited on the surface of these TiO_2 ETLs does not change significantly (Supporting Information, Figure S6). Both TiO_2/perovskite and TiO_2-HCl/perovskite films show similar absorption tendency with the same band gap of perovskite ($E_g=$ 1.634 eV, Figure 3a; Supporting Information, Figure S7 and Note 2). Only a slightly lower absorbance at shorter wavelength was observed for the HCl-treated sample. However, the TiO_2/perovskite film on the FTO glass displays a strong photoluminescence (PL) peak at about 780 nm, while the PL peak intensity quenches largely for the TiO_2-HCl/perovskite film. This result signifies that TiO_2-HCl possesses a stronger electron extraction capability and facilitates more efficient electron transfer from $Cs_{0.06}FA_{0.79}MA_{0.15}Pb(I_{0.85}Br_{0.15})_3$ to TiO_2-HCl. The increased electron density (Figure 2d) and the increased conductivity of the TiO_2-HCl sample account for the suppressed charge recombination at interfaces.[28] The negative impact of the lower absorbance (Figure 3a) for TiO_2-HCl on device performance is offset by the improved electron

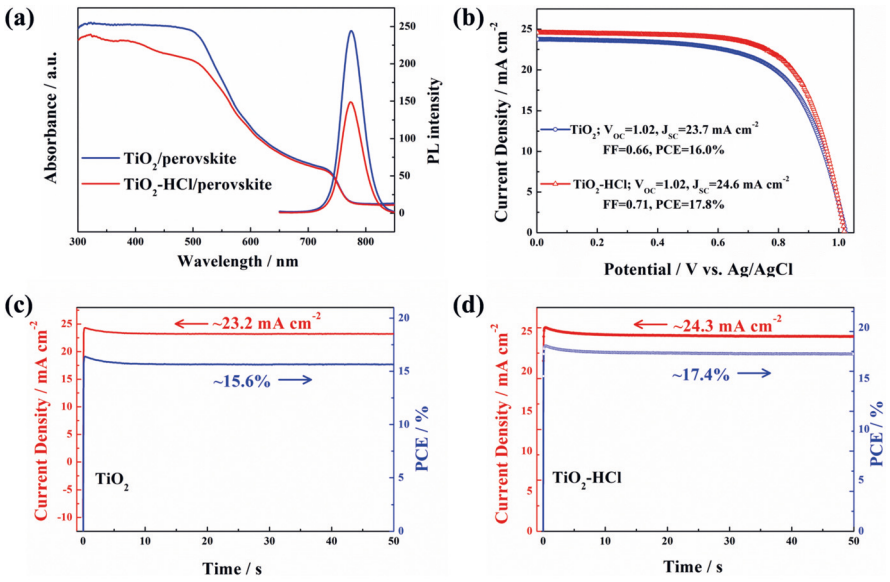

Figure 3. a) UV/Vis absorption and photoluminescence (PL) spectra of the TiO_2/perovskite and TiO_2-HCl/perovskite films. b) The *J–V* characteristics of TiO_2- and TiO_2-HCl-based champion devices. Photocurrent density and the corresponding *PCE* of c) the TiO_2-based and d) TiO_2-HCl-based devices measured as a function time at a constant bias of 0.715 V under an AM1.5G standard sunlight.

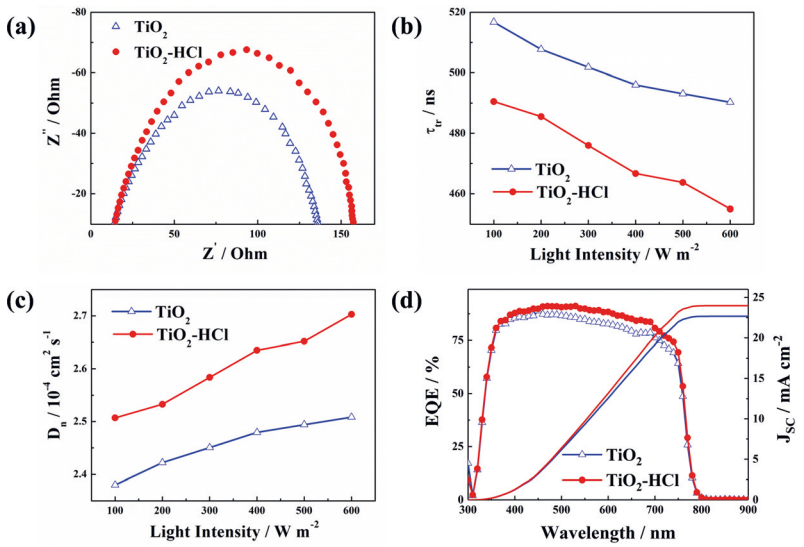

Figure 4. a) Nyquist plots of electrochemical impedance spectroscopy (EIS) for the TiO_2- and TiO_2-HCl-based devices under illumination at applied bias of 0.6 V. The frequency ranges from 10 Hz to 1 MHz at a bias of 0.6 V under AM 1.5 G irradiation. b) Electron transport time τ_{tr} and c) the corresponding electron diffusion coefficient D_n as a function of light intensity for the TiO_2- and TiO_2-HCl-based devices. d) External quantum efficiency (EQE) and integrated J_{SC} of TiO_2-based and TiO_2-HCl-based PSCs.

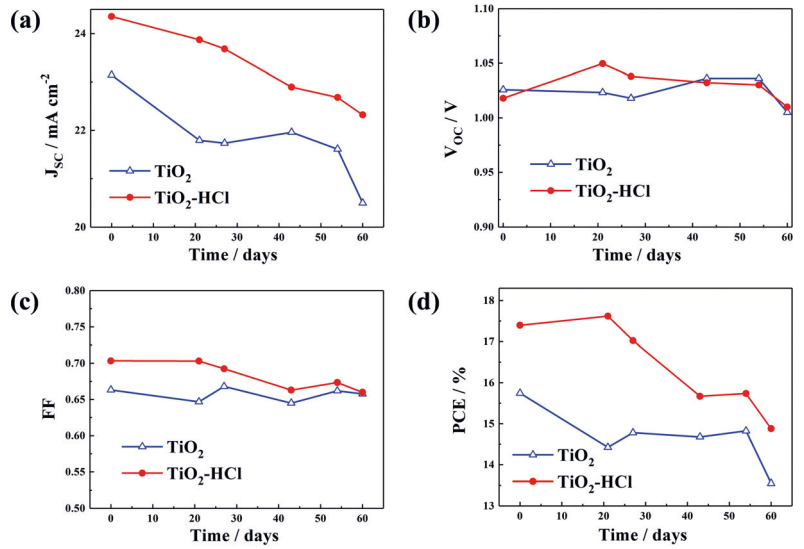

Figure 5. Device stability tests. a) V_{OC}, b) J_{SC}, c) FF and d) PCE as a function of storage time under ambient condition.

transfer of the sample. As a result, compared to that of TiO_2-based counterpart (PCE = 16.0 % of the champion cell), TiO_2-HCl-based PSCs with improved performance (PCE = 17.8 % of the champion cell) were achieved (Figure 3 b). Despite the same open-circuit voltage V_{OC}, the TiO_2-HCl-based device exhibits enhanced J_{SC} and fill factor (FF) owing to the increased donor density and the reduced charge recombination. A stable output photocurrent density of 24.3 mA cm^{-2} and PCE of 17.4 % was obtained in the TiO_2-HCl-based device (Figure 3 d). We note that when replacing $Cs_{0.06}FA_{0.79}MA_{0.15}Pb(I_{0.85}Br_{0.15})_3$ with less stable $MAPbI_3$ as the absorber material, similar trends were observed (that is, PCE = 14.8 % for pristine anatase TiO_2-based $MAPbI_3$ champion solar cell, and PCE = 16.6 % for TiO_2-HCl-based $MAPbI_3$ champion solar cell), as shown in the Supporting Information, Figure S8.

It has been reported that the presence of chlorine can passivate the trap sites at the TiO_2 ETL/perovskite interface.[29] Moreover, the interfacial Cl atoms also improve the binding at the TiO_2/perovskite junction.[30] In our study, Cl 2p spectra are measured to clarify the effect of chlorine on device performance, as shown in Figure 2 f. Chlorine elements were detected on the surface of TiO_2-HCl film without subsequent plasma. However, no characteristic Cl peaks were found in the plasma-treated film. The chlorines are firstly dissociated under the plasma to form Cl free radicals (•Cl), and then escape from the surface of TiO_2.[31] Thus, the defect passivation by interfacial chloride is not applicable in our study. More

importantly, the effects of post-treatment of TiO_2 with HI, HBr, and KCl on the performance of the resulting PSCs were also investigated (Supporting Information, Figure S9). Similar *J–V* curves were seen for these devices (HCl-, HBr- and HI-treated), indicating that the acid anions (Cl^-, Br^-, and I^-) have insignificant impact on the device performance. Notably, the KCl treatment did not yield the device with improved performance, further suggesting that chloride ions have no contribution to the device performance in our work.

We now turn our attention to scrutinize the kinetics of charge transfer at the interface between the perovskite and TiO_2 ETL as well as between the perovskite and TiO_2-HCl ETL. Figure 4 compares the electrochemical impedance spectroscopy (EIS) analysis on the TiO_2- and TiO_2-HCl-based devices. The semicircle at low frequency (high Z') is assigned to the charge recombination resistance, R_{rec}.[32] Clearly, the TiO_2-HCl-based device has a larger R_{rec}, implying that the recombination of electrons and holes at the interface of TiO_2 and perovskite is retarded, which is in good agreement with the PL results (Figure 3a). The electron transport and recombination time of PSCs were further analyzed by controlled intensity-modulated photocurrent spectroscopy (CIMPS), which measures the photocurrent as a function of incident illumination intensity at 0 V bias. Representative Nyquist and Bode plots of CIMPS for the two types of devices are given in the Supporting Information, Figure S10. The electron transport time τ_{tr} can be derived from the CIMPS spectrum (Figure 4b) using the following equation $\tau_{tr} = 1/(2\pi f_{CIMPS})$, where f_{CIMPS} is the maximum frequency at a certain light intensity in each semicircle. The τ_{tr} values of TiO_2-HCl-based device are shorter than those of the control device due to the improved charge transfer capacity of the TiO_2-HCl ETL. The electron diffusion coefficient D_n can be obtained from $D_n = d^2/(2.35\,\tau_{tr})$, where d is the thickness of the TiO_2 photoanode (ca. 150 nm).[33] The D_n of the TiO_2-HCl-based device achieved under different light intensities are higher than the TiO_2-based device (Figure 4c), signifying that the photogenerated electrons can diffuse readily and are collected rapidly from perovskite to the FTO substrate, which effectively suppresses the charge carrier recombination. Consequently, the TiO_2-HCl-based device yields enhanced exterrnal quantum efficiency (EQE, Figure 4d) over the range of 400–750 nm. The integrated photocurrents are in good agreement with the photocurrent values measured from *J–V* curves (Figure 3d).

It is not surprising that acid treatment time would impact the device performance by affecting the corrosion degree of crystalline TiO_2 film and thus altering the carrier transport properties.[34] J_{SC} increases first and then decreases as the acid treatment time progresses (Supporting Information, Figure S11). The devices based on TiO_2 film with a 2 h HCl treatment exhibit the best performance. Obvious cracks were found to form on the surface of TiO_2 after long acid treatment (8 h; Supporting Information, Figure S12), which may cause a direct contact of perovskite and FTO during the deposition of perovskite absorber. The long acid treatment weakens the anatase-amorphous layer interaction due to the breaking of Ti–O–Ti bonds among the chains of amorphous TiO_2 as well as the chains between of amorphous and anatase TiO_2,[11,35] resulting in the detachment of amorphous buffer layer from the anatase TiO_2 ETL and thus decreased electron transport.

Finally, the stability of the TiO_2 ETL-based and TiO_2-HCl ETL-based PSCs was also examined. The devices were stored in a desiccator at temperature of 24 ± 2 °C and a relative humidity of 30 ± 2 % without encapsulation. Figure 5 compares the photovoltaic parameters as a function of time (the initial *J–V* curves are shown in the Supporting Information, Figure S13). Both the two devices experience a drop in J_{SC}. Comparatively, the parameters of FF and V_{OC} are rather stable. The $Cs_{0.06}FA_{0.79}MA_{0.15}Pb(I_{0.85}Br_{0.15})_3$-based device has been shown to be very stable,[36] and it is clear that the HCl-treated TiO_2 as ETL has no adverse impact on the stability of this type of perovskite-based devices.[36] We note that the J_{SC}, V_{OC}, FF, and PCE increased occasionally during storage, which can be ascribed to the oxidation of spiro-MeOTAD layer.[37] Oxidized spiro-MeOTAD facilitates the transport and collection of holes into electrodes, and thus enhances the device performance.

Conclusion

In summary, we developed a viable acid-treatment route to crafting, for the first time, an amorphous, oxygen vacancies-containing TiO_2 buffer layer that is intimately situated on the surface of anatase TiO_2, bridging the interface between the acid-treated TiO_2 ETL and the perovskite absorber, and in turn rendering improved performance of the resulting perovskite solar cells. Notably, oxygen vacancies generated in acid-treated TiO_2 exist both on the surface and in the bulk of TiO_2 nanoparticles. Importantly, subsequent O_2 plasma treatment retains the bulk vacancies while effectively eliminating the surface vacancies. Compared to the pristine TiO_2 ETL, the acid-treated TiO_2 ETL carries an increased electron density and bulk conductivity due to the creation of abundant oxygen vacancies, thereby enabling efficient electron transfer from perovskite to acid-treated TiO_2 ETL and thus suppressing photogenerated electron-hole recombination. This in turn accounts for enhanced J_{SC} and PCE in acid-treated TiO_2 ETL-based devices. The judicious growth of amorphous buffer layer closely positioned on the surface of semiconductor of the same material as ETL may open up a new avenue for design and optimization of efficient ETL for high-performance PSCs.

Acknowledgements

This work is supported by National Science Foundation (ECCS 1914562). B.W. gratefully acknowledges the financial support from the China Scholarship Council, the National Natural Science Foundations of China (21603098, 51673061).

Conflict of interest

The authors declare no conflict of interest.

Keywords: acid treatment · amorphous materials · electron transporting layers · oxygen vacancies · perovskite solar cells

How to cite: *Angew. Chem. Int. Ed.* **2020**, *59*, 1611 – 1618
Angew. Chem. **2020**, *132*, 2 – 1635

[1] a) M. He, D. J. Zheng, M. Y. Wang, C. J. Lin, Z. Q. Lin, *J. Mater. Chem. A* **2014**, *2*, 5994 – 6003; b) L. J. Zuo, Z. W. Gu, T. Ye, W. F. Fu, G. Wu, H. Y. Li, H. Z. Chen, *J. Am. Chem. Soc.* **2015**, *137*, 2674 – 2679.
[2] a) P. R. Cheng, Z. Xu, J. B. Li, Y. C. Liu, Y. Y. Fan, L. Y. Yu, D. M. Smilgies, C. Muller, K. Zhao, S. F. Liu, *ACS Energy Lett.* **2018**, *3*, 1975 – 1982; b) National Renewable Energy Laboratory (NREL), **2019**.
[3] H. P. Zhou, Q. Chen, G. Li, S. Luo, T. B. Song, H. S. Duan, Z. R. Hong, J. B. You, Y. S. Liu, Y. Yang, *Science* **2014**, *345*, 542 – 546.
[4] F. Giordano, A. Abate, J. P. C. Baena, M. Saliba, T. Matsui, S. H. Im, S. M. Zakeeruddin, M. K. Nazeeruddin, A. Hagfeldt, M. Graetzel, *Nat. Commun.* **2016**, *7*, 10379.
[5] a) X. P. Liu, T. L. Bu, J. Li, J. He, T. H. Li, J. Zhang, W. N. Li, Z. L. Ku, Y. Peng, F. Z. Huang, Y. B. Cheng, J. Zhong, *Nano Energy* **2018**, *44*, 34 – 42; b) L. B. Qiu, L. K. Ono, Y. Jiang, M. R. Leyden, S. R. Raga, S. H. Wang, Y. B. Qi, *J. Phys. Chem. B* **2018**, *122*, 511 – 520.
[6] a) D. M. Hausmann, R. G. Gordon, *J. Cryst. Growth* **2003**, *249*, 251 – 261; b) T. S. Sherkar, C. Momblona, L. Gil-Escrig, J. Avila, M. Sessolo, H. J. Bolink, L. J. A. Koster, *ACS Energy Lett.* **2017**, *2*, 1214 – 1222.
[7] Y. R. Hou, J. Y. Yang, Q. H. Jiang, W. X. Li, Z. W. Zhou, X. Li, S. Q. Zhou, *Sol. Energy Mater. Sol. Cells* **2016**, *155*, 101 – 107.
[8] E. Verlage, S. Hu, R. Liu, R. J. R. Jones, K. Sun, C. X. Xiang, N. S. Lewis, H. A. Atwater, *Energy Environ. Sci.* **2015**, *8*, 3166 – 3172.
[9] a) S. Hu, M. R. Shaner, J. A. Beardslee, M. Lichterman, B. S. Brunschwig, N. S. Lewis, *Science* **2014**, *344*, 1005 – 1009; b) M. R. Shaner, S. Hu, K. Sun, N. S. Lewis, *Energy Environ. Sci.* **2015**, *8*, 203 – 207; c) M. J. Torralvo, J. Sanz, I. Sobrados, J. Soria, C. Garlisi, G. Palmisano, S. Cetinkaya, S. Yurdakal, V. Augugliaro, *Appl. Catal. B* **2018**, *221*, 140 – 151; d) J. P. Yang, Y. X. Wang, W. Li, L. J. Wang, Y. C. Fan, W. Jiang, W. Luo, Y. Wang, B. Kong, C. Selomulya, H. K. Liu, S. X. Dou, D. Y. Zhao, *Adv. Mater.* **2017**, *29*, 1700523; e) Z. W. Ren, J. Wang, Z. X. Pan, K. Zhao, H. Zhang, Y. Li, Y. X. Zhao, I. Mora-Sero, J. Bisquert, X. H. Zhong, *Chem. Mater.* **2015**, *27*, 8398 – 8405.
[10] X. H. Lu, G. M. Wang, T. Zhai, M. H. Yu, J. Y. Gan, Y. X. Tong, Y. Li, *Nano Lett.* **2012**, *12*, 1690 – 1696.
[11] G. M. Wang, Y. C. Ling, Y. Li, *Nanoscale* **2012**, *4*, 6682 – 6691.
[12] V. Petkov, G. Holzhuter, U. Troge, T. Gerber, B. Himmel, *J. Non-Cryst. Solids* **1998**, *231*, 17 – 30.
[13] J. Soria, J. Sanz, M. J. Torralvo, I. Sobrados, C. Garlisi, G. Palmisano, S. Cetinkaya, S. Yurdakal, V. Augugliaro, *Appl. Catal. B* **2017**, *210*, 306 – 319.
[14] a) Q. X. Wen, J. Yu, X. Y. Sun, J. Zhuang, Q. G. He, X. You, J. Guo, L. Y. Tao, *New J. Chem.* **2016**, *40*, 3233 – 3237; b) T. Watson, C. Charbonneau, D. Bryant, D. Worsley, *Int. J. Photoenergy* **2012**, *2012*, 637839.
[15] J. W. Zhang, L. L. Zhang, J. W. Zhang, Z. J. Zhang, Z. S. Wu, *J. Alloys Compd.* **2015**, *642*, 28 – 33.
[16] A. Klasen, P. Baumli, Q. Sheng, E. Johannes, S. A. Bretschneider, I. M. Hermes, V. W. Bergmann, C. Gort, A. Axt, S. A. L. Weber, H. Kim, H. J. Butt, W. Tremel, R. Berger, *J. Phys. Chem. C* **2019**, *123*, 13458 – 13466.
[17] X. H. Wang, L. Lu, B. Wang, Z. Xu, Z. Y. Xin, S. C. Yan, Z. R. Geng, Z. G. Zou, *Adv. Funct. Mater.* **2018**, *28*, 1804191.
[18] M. A. Rahman, J. P. Thomas, K. T. Leung, *Adv. Energy Mater.* **2018**, *8*, 1701234.
[19] M. V. Ganduglia-Pirovano, A. Hofmann, J. Sauer, *Surf. Sci. Rep.* **2007**, *62*, 219 – 270.
[20] B. Wang, X. H. Wang, L. Lu, C. G. Zhou, Z. Y. Xi, J. J. Wang, X. K. Ke, G. D. Sheng, S. C. Yan, Z. G. Zou, *ACS Catal.* **2018**, *8*, 516 – 525.
[21] Y. Wang, C. X. Feng, M. Zhang, J. J. Yang, Z. J. Zhang, *Appl. Catal. B* **2010**, *100*, 84 – 90.
[22] X. Y. Xu, C. X. Xu, J. Dai, J. G. Hu, F. J. Li, S. Zhang, *J. Phys. Chem. C* **2012**, *116*, 8813 – 8818.
[23] a) Y. Yang, Y. C. Ling, G. M. Wang, T. Y. Liu, F. X. Wang, T. Zhai, Y. X. Tong, Y. Li, *Nano Lett.* **2015**, *15*, 7051 – 7057; b) J. J. Zhang, X. X. Chang, C. C. Li, A. Li, S. S. Liu, T. Wang, J. L. Gong, *J. Mater. Chem. A* **2018**, *6*, 3350 – 3354; c) F. Zhang, W. Ma, H. Z. Guo, Y. C. Zhao, X. Y. Shan, K. J. Jin, H. Tian, Q. Zhao, D. P. Yu, X. H. Lu, G. Lu, S. Meng, *Chem. Mater.* **2016**, *28*, 802 – 812.
[24] a) Z. Z. Wang, J. Fang, Y. Mi, X. Y. Zhu, H. Ren, X. F. Liu, Y. Yan, *Appl. Surf. Sci.* **2018**, *436*, 596 – 602; b) U. Dasgupta, S. Chatterjee, A. J. Pal, *Sol. Energy Mater. Sol. Cells* **2017**, *172*, 353 – 360.
[25] D. N. Pei, L. Gong, A. Y. Zhang, X. Zhang, J. J. Chen, Y. Mu, H. Q. Yu, *Nat. Commun.* **2015**, *6*, 8696.
[26] H. Elbohy, K. M. Reza, S. Abdulkarim, Q. Q. Qiao, *Sustainable Energy Fuels* **2018**, *2*, 403 – 412.
[27] A. Janotti, J. B. Varley, P. Rinke, N. Umezawa, G. Kresse, C. G. Van de Walle, *Phys. Rev. B* **2010**, *81*, 085212.
[28] G. M. Wang, H. Y. Wang, Y. C. Ling, Y. C. Tang, X. Y. Yang, R. C. Fitzmorris, C. C. Wang, J. Z. Zhang, Y. Li, *Nano Lett.* **2011**, *11*, 3026 – 3033.
[29] H. R. Tan, A. Jain, O. Voznyy, X. Z. Lan, F. P. G. de Arquer, J. Z. Fan, R. Quintero-Bermudez, M. J. Yuan, B. Zhang, Y. C. Zhao, F. J. Fan, P. C. Li, L. N. Quan, Y. B. Zhao, Z. H. Lu, Z. Y. Yang, S. Hoogland, E. H. Sargent, *Science* **2017**, *355*, 722 – 726.
[30] E. Mosconi, E. Ronca, F. De Angelis, *J. Phys. Chem. Lett.* **2014**, *5*, 2619 – 2625.
[31] L. A. Barrie, J. W. Bottenheim, R. C. Schnell, P. J. Crutzen, R. A. Rasmussen, *Nature* **1988**, *334*, 138 – 141.
[32] X. T. Meng, X. Cui, M. Rager, S. G. Zhang, Z. W. Wang, J. Yu, Y. W. Harn, Z. T. Kang, B. K. Wagner, Y. Liu, C. Yu, J. S. Qiu, Z. Q. Lin, *Nano Energy* **2018**, *52*, 123 – 133.
[33] U. Poudyal, F. S. Maloney, K. Sapkota, W. Y. Wang, *Nanotechnology* **2017**, *28*, 415401.
[34] W. J. Ke, G. J. Fang, Q. Liu, L. B. Xiong, P. L. Qin, H. Tao, J. Wang, H. W. Lei, B. R. Li, J. W. Wan, G. Yang, Y. F. Yan, *J. Am. Chem. Soc.* **2015**, *137*, 6730 – 6733.
[35] S. C. Hao, J. H. Wu, L. Q. Fan, Y. F. Huang, H. M. Lin, Y. L. Wei, *Sol. Energy* **2004**, *76*, 745 – 750.
[36] M. Saliba, T. Matsui, J. Y. Seo, K. Domanski, J. P. Correa-Baena, M. K. Nazeeruddin, S. M. Zakeeruddin, W. Tress, A. Abate, A. Hagfeldt, M. Gratzel, *Energy Environ. Sci.* **2016**, *9*, 1989 – 1997.
[37] S. Wang, W. Yuan, Y. S. Meng, *ACS Appl. Mater. Interfaces* **2015**, *7*, 24791 – 24798.

Manuscript received: August 16, 2019
Revised manuscript received: October 29, 2019
Accepted manuscript online: October 30, 2019
Version of record online: November 18, 2019

